

Particle dynamics in two-dimensional random energy landscapes – experiments and simulations

Florian Evers,^{*a} Richard D. L. Hanes,^a Christoph Zunke,^a Jörg Bewerunge,^a Imad Ladadwa,^{b,c} Andreas Heuer,^b and Stefan U. Egelhaaf^a

The dynamics of individual colloidal particles in random potential energy landscapes were investigated experimentally and by Monte Carlo simulations. The value of the potential at each point in the two-dimensional energy landscape follows a Gaussian distribution. The width of the distribution, and hence the degree of roughness of the energy landscape, was varied and its effect on the particle dynamics studied. In the experiments, the energy landscapes were generated optically using a holographic set-up with a spatial light modulator, and the particle trajectories followed by video microscopy. The dynamics are characterized using, e.g., the time-dependent diffusion coefficient, the mean squared displacement, the van Hove function and the non-Gaussian parameter. The dynamics are initially diffusive, show an extended sub-diffusive regime at intermediate times before diffusive motion is recovered at very long times. Compared to the dynamics in a one-dimensional potential energy landscape, the localization at intermediate times is weaker and the diffusive regime at long times reached earlier, which is due to the possibility to avoid local maxima in two-dimensional energy landscapes.

1 Introduction

The Brownian motion of colloidal particles is one of the classical phenomena in statistical physics.^{1,2,3} In real situations, the particles often do not move freely, but their dynamics are modified by an external potential.^{4,5,6} Especially a random potential, and thus Brownian motion in the presence of disorder, leads to interesting transport phenomena.^{7,8} Up to now, the dynamics in random potentials have been studied mainly by theory and computer simulations.^{9,10,11,12,13,14,15} Theoretical models include the random barrier model,¹² the random trap model,¹³ the random walk with barriers¹⁴ and the continuous time random walk¹⁵ as well as studies of diffusion in a rough potential¹⁶ and in materials with defects like zeolites.¹⁷ In particular the long-time limit has been investigated for different realizations of random potentials.^{7,8} In contrast, less is known on the intermediate regime and the time needed to reach the long-time limit. To our knowledge, only very few systematic experimental tests of theoretical and simulation predictions have been performed.^{18,19,20} Nevertheless, the theoretical predictions have been applied successfully to experimental data and the concept of particles diffusing through an energy landscape has proven very useful in understanding very different phenomena. This includes particle diffusion in inhomogeneous media (e.g. single molecule dynamics in porous gels²¹ or in cells^{22,23,24}), the dynamics on rough surfaces,^{25,26} the dynamics of particles moving along the walls

between magnetic domains,^{18,27} the dynamics of independent charge carriers in a conductor with impurities (in the parameter range where conduction can be modeled as a classical process).^{28,29} Furthermore, some processes can be represented by diffusion in the systems' configuration space, for example vitrification leading to glassy systems^{30,31,32,33,34,35} or protein folding.^{36,37,38,39,40} Often diffusion in a potential energy landscape represents a crude approximation only, but it can nevertheless provide a useful first description of the effect of disorder on the dynamics. Disorder may modify the value of the diffusion coefficient or it may alter Brownian motion leading to anomalous diffusion. Which effect dominates depends not only on the specific process, but also on the time scale of interest.

An external potential can be imposed on a polarizable colloidal particle by exposing it to a light field.^{41,42,43,44} Light exerts different forces on particles, if their refractive index differs from (typically exceeds) that of the solvent: a scattering force or 'radiation pressure', which pushes particles along the laser beam, and a gradient force, which attracts particles toward regions of high light intensity.^{41,42,43} A classical application of this effect are optical tweezers which are used to trap individual particles by a tightly focused laser beam.^{41,42,43,45,46,47} Furthermore, above a certain light intensity, a periodic light field can induce a disorder-order transition in a two-dimensional charged colloidal system, known as light-induced freezing, and, if the intensity is increased further, the induced crystal melts into a modulated liquid, called light-induced melting.^{48,49,50} In addition to the particle arrangement, the particle dynamics can be affected by periodic⁵¹ and random¹⁹ light fields, resulting in anomalous diffusion. Light

^a Condensed Matter Physics Laboratory, Heinrich-Heine-University, Universitätsstraße 1, D-40225 Düsseldorf, Germany. E-mail: florian.evers@hhu.de

^b Institut für Physikalische Chemie, Universität Münster, D-48149 Münster, Germany

^c Fahad Bin Sultan University, SA-71454 Tabuk, Saudi-Arabia

fields hence provide a means to manipulate the spatial arrangement and dynamics of colloidal particles.

Recently, we experimentally realized one-dimensional random energy landscapes^{19,45} and periodic potentials^{44,51} using laser light fields and studied the dynamics of individual particles in these potentials. Here, this is extended to the dynamics of individual colloidal particles in two-dimensional random potentials. In our experiments and simulations, the values of the two-dimensional random potential were drawn from a Gaussian distribution, whose width ϵ represents the degree of roughness of the potential and in the experiments was controlled by the laser power P . The static properties of the potential were determined quantitatively. Furthermore, the trajectories of individual particles in this potential were followed using video microscopy,^{52,53,54} and compared to our simulation results. The dynamics were characterized by, e.g., the time-dependent diffusion coefficient, the mean squared displacement (MSD), the non-Gaussian parameter, and the van Hove function. The dynamics are initially diffusive but then, at intermediate times, show an extended subdiffusive regime before diffusive behaviour is reestablished at very long times. Our findings are compared to the particle dynamics in one-dimensional random potentials^{19,20} and periodic potentials.⁵¹ Two dimensions allows particles to bypass large barriers. Therefore, the particle dynamics are controlled by minima and saddle points instead of minima and maxima. Moreover, compared to periodic potentials the barriers have different heights. This significantly affects the particle dynamics, for example the dependence of the dynamics on the degree of roughness of the potential is modified.

2 Materials and methods

2.1 Sample preparation

Each sample consisted of surfactant-free sulfonated polystyrene (PS) particles with a radius $R = 1.4 \mu\text{m}$ and polydispersity 3.2 % (Interfacial Dynamics Microspheres & Nanospheres) suspended in heavy water (D_2O), so that the particles cream rather than sediment. Stock solutions of the particles were diluted to result in an area fraction of the creamed sample, $\sigma < 0.10$, which represents a compromise between negligible particle-particle interactions and reasonable statistics. Area fractions were estimated from micrographs according to $\sigma = \pi R^2 N_p / A$ with N_p and A being the number of particles and the area covered by the light field, respectively.

The heavy water (D_2O) was de-ionised by stirring with ion exchange resin to increase the particle-glass repulsion and thus reduce the fraction of particles sticking to the glass surface. To further reduce sticking, all glassware was sonicated in 2% Helmanex II solution at about 60 °C and then rinsed with Mil-

lipore water and dried in air prior to use. Each sample cell was constructed from a microscope slide and three cover slips, two used as spacers (number 0 with thickness 0.085 – 0.13 mm, supplied by VWR) with a gap between them and the third on top to create a narrow capillary (number 1 with thickness 0.13 – 0.16 mm, supplied by VWR).⁵⁵ Thin cover glasses were used as spacers to allow imaging of the creamed particles using a high resolution objective with a working distance of 0.13 mm. The sample chamber was filled using capillary action and subsequently sealed with UV glue.

2.2 Light field generation

The set-up contains a laser with a wavelength of 532 nm (Ventus 532-1500, Laser Quantum). Its beam is expanded and then reflected from a spatial light modulator (Holoeye 2500-LCR). Subsequently it is directed through two telescopes to reduce its diameter and reflected off three mirrors to steer it through an inverted microscope (Nikon Eclipse 2000-U) into the sample.^{19,45} One of the mirrors is a dichroic mirror to introduce the beam into the microscope beam path and to use the microscope objective (60 \times oil immersion, numerical aperture NA 1.4, Nikon) to image the light field into the sample plane. The beam passes upwards through the sample and hence, due to radiation pressure, pushes the particles against the top of the cell, which reinforces the creaming of the particles. A notch filter in the imaging path prevents laser light from reaching the ocular or camera. To aid alignment, the notch filter can be removed and the sample replaced by a mirror, so that the light intensity distribution in the sample plane can be imaged using the microscope.

A kinoform (phase hologram) was calculated using the Gerchberg-Saxton iterative algorithm⁵⁶ (Fig. 1A) and displayed in the centre of the spatial light modulator. The kinoform corresponds to a homogeneous disc surrounded by a ring to prevent particle movements into and out of the disc. The Fourier transform of the kinoform is, as expected, a homogeneous disc surrounded by a ring (Fig. 1B). In order to account for the angle at which the laser impinges on the spatial light modulator (22.5°), the disc and ring are a factor $1/\cos(22.5^\circ) = 1.08$ taller than they are wide.^{19,45} The observed light field intensity $I(x,y)$ (Fig. 1C) corresponds to the disc of the Fourier transformed kinoform. Indeed, the illumination is overall flat but, crucially, has some fluctuations due to the finite size and pixelation of the light modulator.¹⁹ These fluctuations are exploited in the following. Furthermore, there is a bright 0th-order peak in the centre. Using this peak, a particle was trapped and used to monitor any drift of the set-up.¹⁹ Global drifts were found to be negligible during individual measurements (up to 4 h).

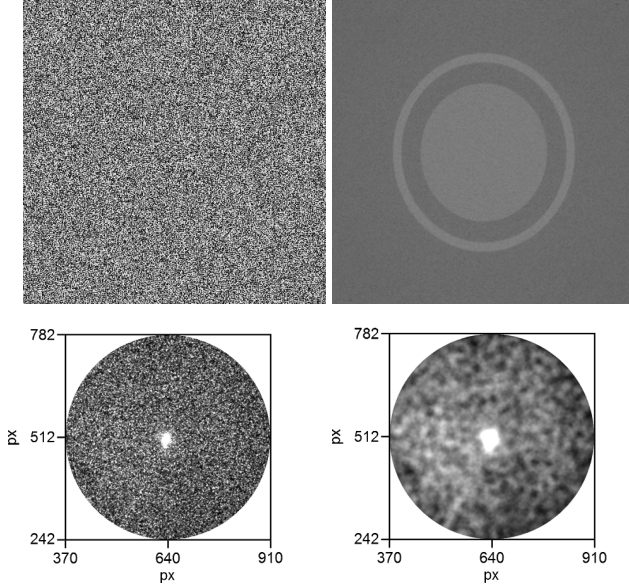


Fig. 1 (A) Kinoform calculated by applying the Gerchberg-Saxton algorithm to a homogeneous disc surrounded by a ring and (B) its Fourier transform. (C) Micrograph of the observed intensity $I(x,y)$ of the disc taken at very low laser power $P \leq 0.2$ mW. (D) Potential $U(x,y)$ as experienced by a point-like test particle obtained by convoluting $I(x,y)$ with the volume of a spherical particle with radius $R = 1.4 \mu\text{m} \hat{=} 12.7$ pixels.

2.3 Video microscopy and particle tracking

The samples were observed using the inverted microscope. Micrographs were recorded using a CMOS camera (PL-B742F, Pixelink). Particle coordinates were extracted from the time series of micrographs and the trajectories determined using IDL routines.⁵² Typical measurement times were 2 to 4 h. Particles which were stuck to the glass were identified by comparing the particles' short-time friction coefficient ξ_j , i.e. the inverse mobility, determined from the mean squared displacement, to the expected bulk value $\xi_0 = 6\pi\eta R$, with the solvent viscosity $\eta = 1.19 \times 10^{-3}$ Pas at room temperature. Particles with $\xi_j > 20\xi_0$ were declared stuck and removed from the analysis. Typically, one particle was stuck to the glass in the field of view, which contained about 20 particles.

For identical conditions, measurements at different positions in the sample yielded very similar results, despite slightly different particle area fractions σ . This reproducibility allowed us to average several independent measurements to improve statistics.

2.4 Monte Carlo simulations

The Monte Carlo simulations were performed on a 4096×4096 square lattice with the lattice points separated by Δs in

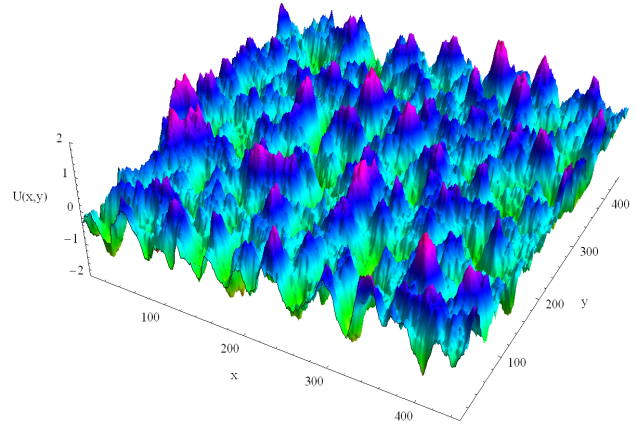


Fig. 2 Some region of the spatially correlated Gaussian potential energy landscape $U(x,y)$, obtained by convolution of a spatially uncorrelated Gaussian energy landscape with the particle volume. It is used in the Monte Carlo simulations and reflects the potential felt by a particle (Fig. 1D).

both directions, where we have set $\Delta s = 1$. The potential values at the lattice points, $\tilde{U}(x,y)$, were produced using a Box-Muller algorithm generating numbers which are Gaussian distributed with zero mean and standard deviation $\tilde{\epsilon}$. The potential $\tilde{U}(x,y)$ was convoluted with the particle volume to obtain the potential $U(x,y)$ felt by a point-like test particle

$$U(x,y) = \frac{\sum_k \sum_l \tilde{U}(x-k\Delta s, y-l\Delta s) a(k,l)}{\sqrt{\sum_k \sum_l a^2(k,l)}} \quad (1)$$

where the double sum runs over the projected particle, i.e. $k^2 + l^2 \leq m^2$ with $k\Delta s$ and $l\Delta s$ the distances from the particle centre in the two directions and $R = m\Delta s$ the radius of the particle. The volume of the particle is represented by

$$a(k,l) = 2\sqrt{(m^2 - k^2 - l^2)} \quad (2)$$

As a compromise between negligible discretization effects and viable computation time, we have chosen $m = 32$ and thus $-32 \leq k, l \leq 32$ with $k^2 + l^2 \leq m^2$.

The convolution leads to a potential $U(x,y)$ (Fig. 2), which is smoother than $\tilde{U}(x,y)$. Its values follow the same Gaussian distribution, albeit with a spatial correlation decaying on the length scale of the particle size. It is supposed to resemble the potential energy landscape experienced by a colloidal particle in the light field (Sec. 3.1).

Once the potential energy landscape $U(x,y)$ was fixed, a particle was set on a randomly chosen lattice point. During the simulation, a direction is chosen randomly and, depending on

the energy difference ΔU to the neighbouring lattice point, the particle is moved in any case if $\Delta U \leq 0$, or moved with a finite probability $\exp(-\Delta U/k_B T)$ if $\Delta U > 0$. By averaging over 1024 different positions of the particle, representative averages can be determined. For each Monte Carlo run, the short-time diffusion coefficient D_0 and the related Brownian time $t_B = R^2/4D_0$ were calculated. In analogy to the experiment, data were acquired up to $10^3 t_B$. This yielded particle trajectories as in the experiments. Thus, the different parameters, such as the mean squared displacement, were determined as in the experiments and are described below. It turned out that within statistical errors the results for different realizations of the potential energy landscape $U(x, y)$ are identical. Moreover, as in the experiments, separate simulations were performed for different values of the degree of roughness $0 k_B T \leq \varepsilon \leq 5 k_B T$ in steps of $0.25 k_B T$ to investigate its effect on the dynamics.

3 Results and discussion

We studied the behaviour of individual colloidal particles in two-dimensional random potential energy landscapes. At first, the properties of the experimentally created energy landscapes are presented. Then, the particle dynamics in these energy landscapes are discussed and compared to the results of our Monte Carlo simulations. Finally, our experimental and simulation results are contrasted to the dynamics in one-dimensional random and periodic potentials.

3.1 Properties of the optically generated random potential

A realization of the light field at very low laser power is displayed in Fig. 1C. The light field interacts with polarizable particles.^{41,42,43} The polarizable particle volume is taken into account by convolving the local light intensity $I(x, y)$ with the particle volume. The effect of the light field on the particle is then represented by an external potential $U(x, y)$ as felt by a point-like test particle (Fig. 1D). Due to the convolution with the particle volume, the potential is not only proportional to the laser power P , but also to the particle volume, $U \propto PR^3$.

To determine the characteristic length scales of the light field intensity $I(x, y)$ and of the potential felt by a point-like test particle $U(x, y)$, the spatial correlation functions were determined. Based on the two-dimensional intensity distribution $I(x, y)$, the azimuthal average of the two-dimensional spatial correlation function $\langle \Phi(\tilde{x}, \tilde{y}) \rangle_\Omega$ were calculated. The spatial correlation of the light field intensity $I(x, y)$ decays on a short length scale compared to the particle size. However, the convolution with the particle volume introduces a length scale, namely the particle diameter $2R$. The spatial correlation of the potential $U(x, y)$, which was similarly determined, indeed decays on a characteristic length of $2R$ (Fig. 3).

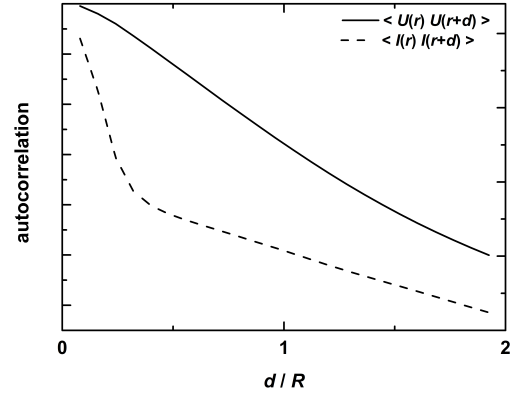


Fig. 3 Azimuthally averaged spatial correlation functions of the laser intensity $I(x, y)$ (dashed line) and of the potential energy landscape felt by a point-like test particle $U(x, y)$ (solid line) as determined from Fig. 1C and D, respectively.

Based on the observed light intensity $I(x, y)$ and potential energy landscape $U(x, y)$ (Fig. 1C,D), the distributions of the light intensity values $p(I)$ and potential values $p(U)$ were determined (Fig. 4). The distribution $p(I)$ follows a Gamma distribution⁵⁷

$$f_\Gamma(I) = \frac{b^k}{\Gamma(k)} I^{k-1} e^{-bI}, \quad (3)$$

where $I \geq 0$ and $\Gamma(k)$ is the Gamma function. A fit to the experimental $p(I)$ yielded $k = 3.1 \pm 0.1$ (Fig. 4A), corresponding to a 3D speckle pattern.^{57,58} The distribution $p(U)$ can be described by a Gaussian distribution

$$f_G(U) = \frac{1}{\sqrt{2\pi}\varepsilon^2} e^{-\frac{(U-\langle U \rangle)^2}{2\varepsilon^2}} \quad (4)$$

with the average $\langle U \rangle$ and width or standard deviation ε (Fig. 4B). Due to the convolution with the particle volume, $U(x, y)$ represents a weighted average of several independent (random) values of $I(x, y)$ and thus $p(U)$ has a significantly reduced width compared to $p(I)$. The width ε characterizes the degree of roughness of the random potential $U(x, y)$, which is controlled by the laser power P , but cannot be easily determined experimentally. Thus, to establish a quantitative relation between the roughness ε , used in the simulations, and the laser power P , applied in experiments, the experimental potential energy landscape needs to be calibrated. This was achieved by a direct comparison of the experimental and simulation results, namely of the time-dependent diffusion coefficient $D(t)$ at very short and long times, and will be described below (Sec. 3.3). The calibration resulted in an approximately linear relation between ε and P , which might saturate for large P (Fig. 5).

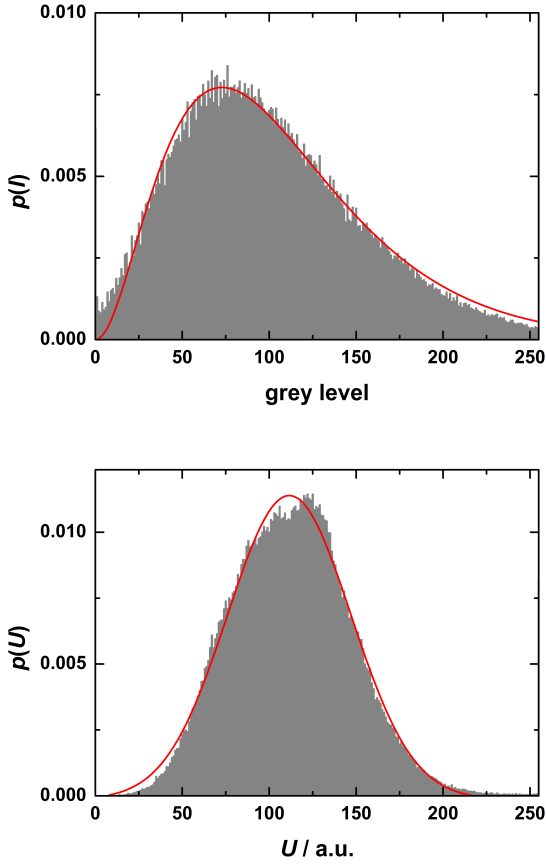


Fig. 4 Distribution of (A) values of the intensity of the light field, $p(I)$, and (B) values of the potential as felt by a point-like test particle, $p(U)$ based on the observed intensity $I(x,y)$ and potential $U(x,y)$ shown in Fig. 1C and D, respectively. Red lines are fits based on a Gamma and Gaussian distribution, respectively.

3.2 Dynamics in the random potential – experiments

The effect of two-dimensional random energy landscapes on the particle dynamics is qualitatively illustrated in Fig. 6. Outside the light field (white background), particles undergo free diffusion, exploring a large area. Separated from this region by a large barrier (white/green rings) is the two-dimensional random light field (green disc). Within the random potential, the excursions of the particles are limited and the particle dynamics hence are slowed down. The particles remain longer at some positions, which correspond to local minima of the potential. For a potential with a larger degree of roughness ε , i.e. a larger width of $p(U)$, this effect is more pronounced with particles being more efficiently trapped and hence exploring a smaller region.

Based on the particle trajectories, different statistical properties were computed to characterize the particle dynamics.

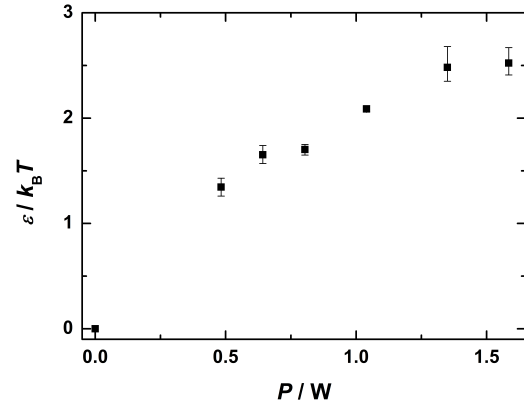


Fig. 5 Standard deviation ε of the distribution of potential energy values, $p(U)$, as a function of laser power P .

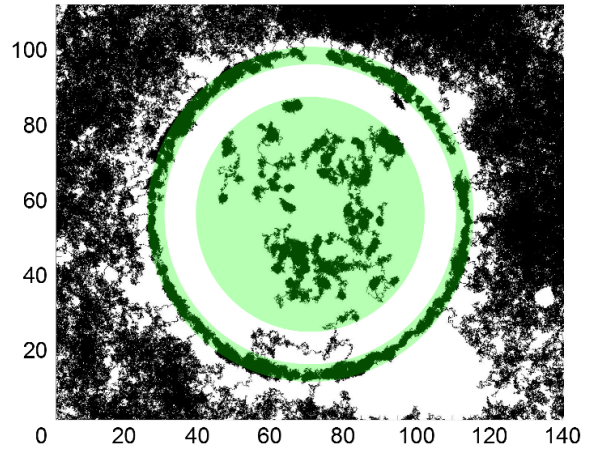


Fig. 6 Trajectories of particles undergoing diffusion in a two-dimensional plane, part of which contains a random potential (green background) which is separated by a barrier (white/green rings) from the surroundings (white background). Particle radius $R = 1.4 \mu\text{m}$, particle surface fraction $\sigma = 0.04$, laser power $P = 1.32 \text{ W}$ corresponding to a standard deviation $\varepsilon = 2.5 k_B T$, and a recording time $T = 3.8 \text{ h}$. Coordinates are given in μm .

We found identical behaviour along the x - and y -directions as expected for an isotropic system. The dynamical properties were hence determined as a function of the distance, $\Delta r = [(\Delta x)^2 + (\Delta y)^2]^{1/2}$, where distances are scaled by the particle radius $R = 1.4 \mu\text{m}$ and times by the Brownian time $t_B = R^2/(4D_0) = (6.3 \pm 0.1) \text{ s}$ (values refer to the experimental system; D_0 has been determined in the absence of a random potential, i.e. $\varepsilon = 0$, but in the vicinity of the water–glass interface). This renders the data independent of the specific experimental conditions. Moreover, the statistical properties were obtained by averaging over different particles, which are

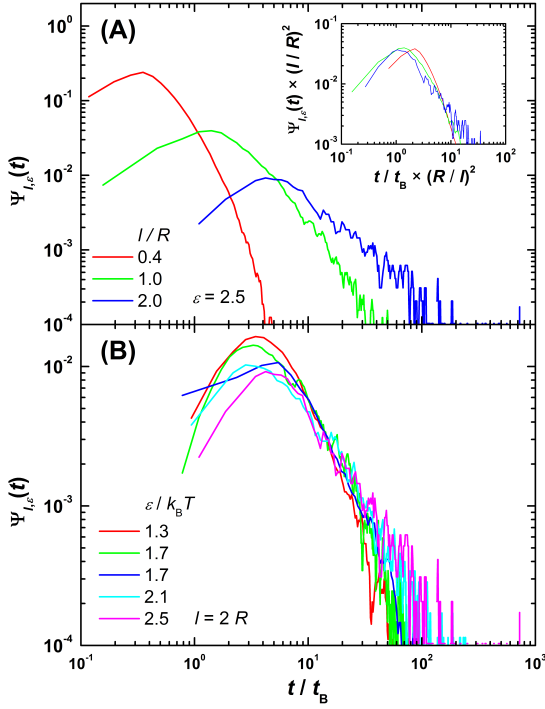


Fig. 7 Particle residence time distribution $\Psi_{l,\varepsilon}(t)$ representing the probability that it takes a particle a time t/t_B to travel at least a distance l in a random potential with standard deviation ε . All curves are smoothed by a moving five-points average. (A) $\Psi_{l,\varepsilon}(t)$ for different length l/R (as indicated) and $\varepsilon = 2.5 k_B T$, scaled plot as inset. (B) $\Psi_{l,\varepsilon}(t)$ for $l/R = 2$ and different ε (as indicated).

non-interacting and thus independent, and waiting times t_0 to improve statistics. Since initially the particles were homogeneously distributed, in the experiments and simulations, but tended toward a Boltzmann distribution in the course of the experiment or simulation, the average over waiting times depends on the total measurement or simulation time T , which was $T \approx 1000 t_B$.

Depending on the particle positions, the particles experience various potential values $U(x, y)$ and are trapped for different times, reflecting the different heights of the saddle points to the neighbouring minima. The time t required to explore at least a distance l in a potential with roughness ε has been determined and the particle residence time distribution $\Psi_{l,\varepsilon}(t)$ determined. To explore a distance l by free diffusion with diffusion coefficient D_0 , on average the time $t_0 = l^2/(4D_0)$ is required. To explore larger distances l and/or in the presence of a random potential, on average larger times are required (Fig. 7A). For short distances $l < 2R$, i.e. within a minimum, $\Psi_{l,\varepsilon}(t)$ does not significantly depend on ε . However, to travel a characteristic length $2R$, which corresponds to the typ-

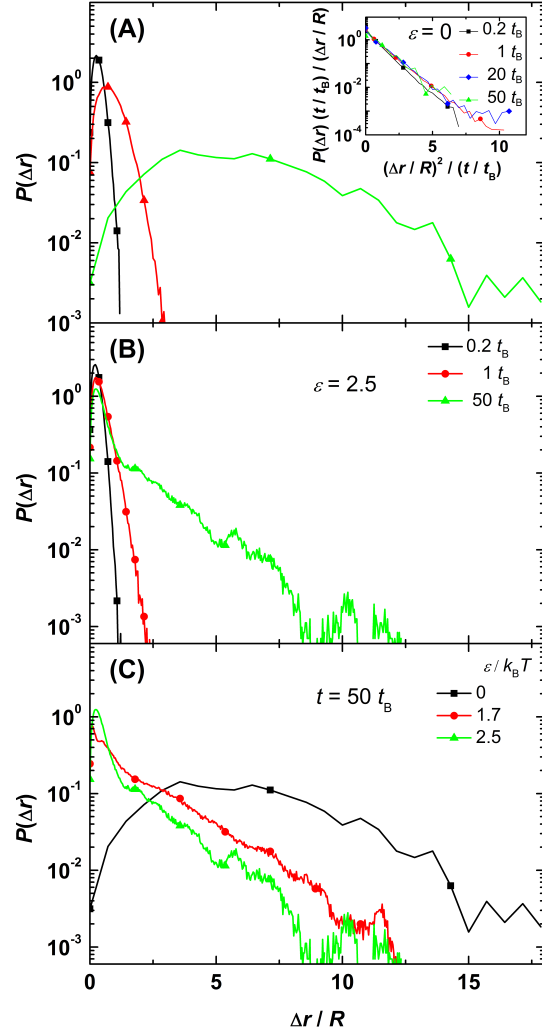


Fig. 8 Distribution of particle displacements Δr within time t , $P(\Delta r, t)$ for (A) free diffusion, i.e. without potential ($\varepsilon = 0$), scaled $P(\Delta r, t)$ as an inset, (B) dynamics in the presence of a random potential with roughness $\varepsilon = 2.5 k_B T$ for different times t (as indicated) and (C) with different roughnesses ε (as indicated) for time $t = 50 t_B$.

ical minimum-minimum separation (Fig. 3), on average a time $t = 4t_B = R^2/D_0$ is required and, in the presence of a random potential, the distribution $\Psi_{l,\varepsilon}(t)$ depends on the roughness ε (Fig. 7B), since a barrier or saddle point, whose average height depends on ε , has typically to be crossed to travel a distance $l > 2R$.

The probability distribution of particle displacements Δr , i.e. the self part of the van Hove function, $P(\Delta r, t)$, at different delay times t is calculated based on the trajectories by averag-

ing over all waiting times t_0 and particles i

$$P(\Delta r, t) = \langle \delta(\Delta r - [r_i(t_0 + t) - r_i(t_0)]) \rangle_{t_0, i}, \quad (5)$$

where $r_i(t)$ is the position of particle i at time t . In the case of free two-dimensional diffusion, i.e. without any external potential, $P(\Delta r, t)$ follows a Rayleigh distribution, $P(\Delta r, t) \sim \Delta r / (2D_0 t) \exp(-\Delta r^2 / 4D_0 t)$, whose width increases linearly with time t (Fig. 8A). In the presence of a random potential, $P(\Delta r, t)$ changes qualitatively (Fig. 8B). The potential tends to trap the particle so that it explores less space and the distributions $P(\Delta r, t)$ get much narrower. This is more pronounced for longer times, when the dynamics include barrier crossing. Accordingly, at long delay times, the roughness of the potential significantly effects $P(\Delta r, t)$, which becomes narrower with increasing ε (Fig. 8C).

The width of the distribution of particle displacements, $P(\Delta r, t)$, can be characterized by the mean squared displacement (MSD)

$$\langle \Delta r^2(t) \rangle_{t_0, i} = \langle [r_i(t_0 + t) - r_i(t_0)]^2 \rangle_{t_0, i} \quad (6)$$

$$= \langle \Delta x^2(t) \rangle_{t_0, i} + \langle \Delta y^2(t) \rangle_{t_0, i}, \quad (7)$$

where $\langle \Delta x^2(t) \rangle = \langle x^2(t) \rangle - \langle x(t) \rangle^2$ and $\langle \Delta y^2(t) \rangle$ is calculated correspondingly. The particle dynamics, as reflected in the MSDs, exhibit three distinct regimes (Fig. 9A). Both, at short times ($t/t_B \lesssim 0.1$) and long times ($t/t_B \gtrsim 30$), the particle dynamics are diffusive. At small t , the diffusive behaviour reflects small excursions within local minima and is thus essentially independent of the roughness ε . (Nevertheless, diffusion at short times is reduced compared to free diffusion ($\varepsilon = 0$), because averages over waiting times t_0 are considered and laser pressure pushes the particles closer to the water-glass interface and thus reduces their mobility,^{59,60,61} with only a very weak apparent dependence on laser power $P > 0$ and hence $\varepsilon > 0$; see Sec. 3.3.) For large enough t , hopping between minima becomes important and constitutes a random walk. Thus diffusive behaviour is reestablished at long times, although with a strongly reduced diffusion coefficient. At intermediate t , the MSDs exhibit an inflection point, which becomes increasingly pronounced as ε increases. This subdiffusive behaviour is caused by the particle being trapped in local minima for prolonged times before it escapes to a neighbouring minima. Since there is a wide range of residence times (Fig. 7), reflecting barriers of different heights, the subdiffusive regime extends over a broad range of times.

From the two-dimensional MSD $\langle \Delta r^2(t) \rangle$, the time-dependent diffusion coefficient $D(t)$ can be calculated according to

$$D(t) = \frac{1}{2d} \frac{\partial}{\partial t} \langle \Delta r^2(t) \rangle_{t_0, i}, \quad (8)$$

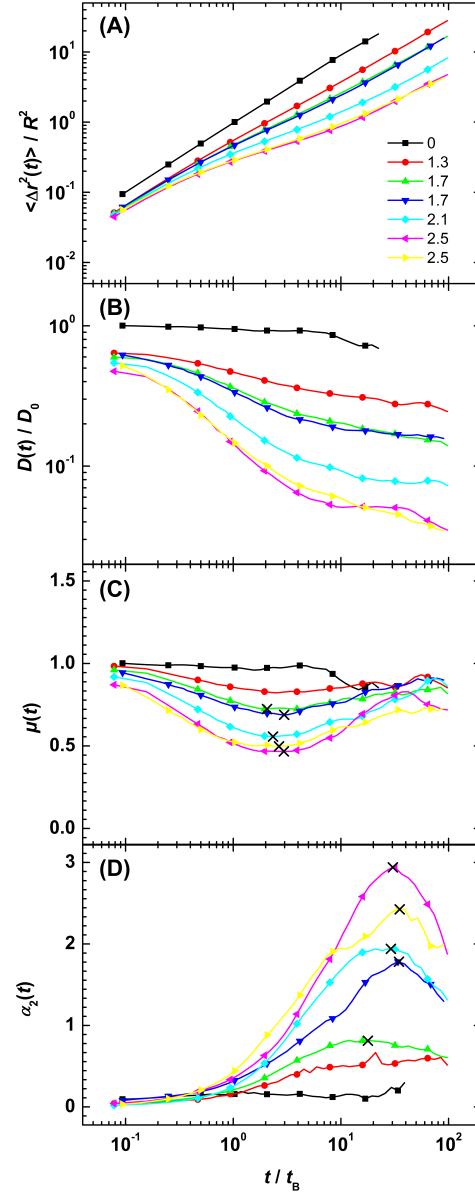


Fig. 9 Particle dynamics in a two-dimensional random potential energy landscape with increasing degrees of roughness ε (as indicated): (A) normalized mean squared displacement $\langle \Delta r^2(t) \rangle / R^2$, (B) normalized diffusion coefficient $D(t) / D_0$, (C) exponent $\mu(t)$ in the relation $\langle \Delta r^2(t) \rangle \propto t^\mu$, and (D) non-Gaussian parameter $\alpha_2(t)$ as a function of delay time t normalized by the Brownian time t_B . For clarity, only every fifth data point is plotted as a symbol. Black crosses indicate minima and maxima of $\mu(t)$ and $\alpha_2(t)$, respectively.

where here the dimension $d = 2$. The three regimes discussed above are also reflected in the normalized time-dependent dif-

fusion coefficient $D(t)/D_0$ (Fig. 9B). Toward very short times, $D(t)/D_0$ tends toward one (actually slightly below one due to the averaging and the radiation pressure discussed above and in Sec. 3.3). It strongly decreases at intermediate times to reach a much smaller value D_∞ at long times, where hopping between minima dominates and diffusion is reestablished, reflected in the plateau of $D(t)$. The long-time regime is experimentally accessible and hence the asymptotic diffusion coefficient D_∞ can be determined experimentally and will be discussed together with the simulation results (Sec. 3.3).

In order to characterize deviations from diffusive behaviour, in particular the subdiffusion at intermediate times, the exponent μ in the relation $\langle \Delta r^2(t) \rangle \sim t^\mu$ is considered. For free diffusion $\mu = 1$, while $\mu < 1$ in the case of subdiffusion. The time-dependence of $\mu(t)$ is calculated from the slope of the MSD in double-logarithmic representation:

$$\mu(t) = \frac{\partial \log \left(\langle \Delta r^2(t) \rangle_{t_0,i} \right)}{\partial \log(t)}. \quad (9)$$

The subdiffusive dynamics at intermediate times cause a minimum in $\mu(t)$, which becomes more pronounced with increasing ε , but remains at about the same time t_μ (Fig. 9C, crosses). In contrast, the diffusive behaviour at short and long times is reflected in the trend of $\mu(t)$ tending toward one for the two limits.

While the exponent $\mu(t)$ characterizes deviations from diffusive behaviour, the non-Gaussian parameter $\alpha_2(t)$ quantifies the deviation of the distribution of particle displacements, $P(\Delta r, t)$, from a Gaussian distribution (Fig. 8). It corresponds to the first non-Gaussian correction to $P(\Delta r, t)$.³⁵ Following a previous definition:⁶²

$$\alpha_2(t) = \frac{\langle \Delta r^4(t) \rangle_{t_0,i}}{(1 + 2/d) \langle \Delta r^2(t) \rangle_{t_0,i}^2} - 1, \quad (10)$$

where $\langle \Delta r^4(t) \rangle = \langle \Delta x^4(t) \rangle + \langle \Delta y^4(t) \rangle + 2 \langle \Delta x^2(t) \rangle \langle \Delta y^2(t) \rangle$ and $\langle \Delta x^4(t) \rangle$ and $\langle \Delta y^4(t) \rangle$ are defined in analogy to $\langle \Delta x^2(t) \rangle$. The time-dependence of $\alpha_2(t)$ also shows three different dynamic regimes (Fig. 9D). At very short and very long times, when the particle dynamics are diffusive, $\alpha_2(t) \approx 0$, while at intermediate times $\alpha_2(t)$ develops a peak which becomes more pronounced and moves to larger t_α with increasing ε . This reflects the broader distribution of barrier heights and hence residence times $\Psi_{l,\varepsilon}(t)$ at larger ε (Fig. 7).

The intermediate regime is hence characterized by subdiffusive dynamics with a minimum in the exponent $\mu(t)$ and, at later times, a maximum in the non-Gaussian parameter $\alpha_2(t)$ (Fig. 9C,D). While the position of the minimum in $\mu(t)$, i.e. the time t_μ hardly depends on ε , the maximum in $\alpha_2(t)$ shifts to larger times t_α with increasing ε (Fig. 10).

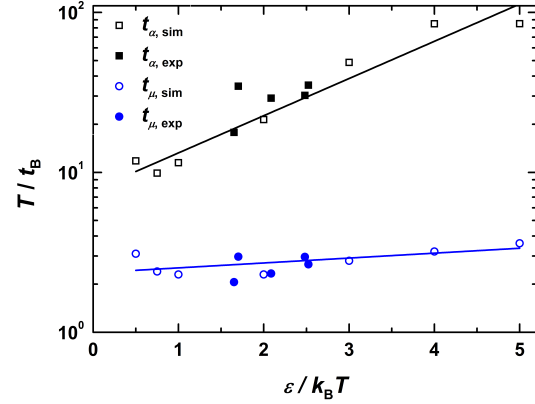


Fig. 10 Characteristic times, namely of the minimum in the exponent $\mu(t)$, i.e. t_μ , and the maximum in the non-Gaussian parameter $\alpha_2(t)$, i.e. t_α , as a function of the degree of roughness ε of the potential energy landscapes from simulations (open symbols) and experiments (filled symbols, corresponding to the crosses in Fig. 9C,D). Solid lines are guides to the eye.

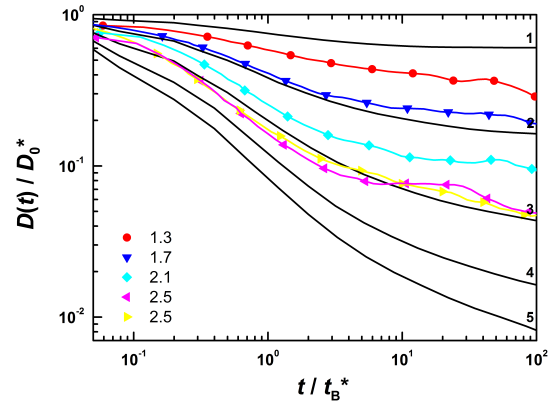


Fig. 11 Normalized diffusion coefficient, $D(t)/D_0$, as a function of delay time t for particles in a two-dimensional random potential energy landscape as observed in simulations (black solid lines, roughness ε as indicated) and experiments (coloured lines with symbols, roughness ε as indicated). To account for the effect of radiation pressure on the particle mobility, the experiments are scaled with an effective Brownian time t_B^* and an effective diffusion coefficient D_0^* as explained in the main text.

3.3 Dynamics in the random potential – simulations

The experimental findings, namely the time-dependent diffusion coefficient $D(t)$, will be compared to simulation results. The degree of roughness ε of the optically-generated potential $U(x,y)$ is tuned via the laser power P , but ε cannot be

determined experimentally. Thus, the relation between the roughness ε and the laser power P needs to be determined by a comparison of the simulation and experimental findings. The diffusion coefficient $D(t)$ exhibits well-developed plateaus at early and late times, $D_s = D(t_s)$ and D_∞ , which depend on ε (in the simulations) and P (in the experiments). Therefore we use the ratio D_∞/D_s determined in simulations (Fig. 12A) to assign an ε to the D_∞/D_s which have been determined experimentally using different P . This yields a relation between roughness and laser power, i.e. $\varepsilon(P)$ (Fig. 5), which appears linear up to large P , where ε starts to saturate. Also other procedures have been followed to determine $\varepsilon(P)$; they all resulted in an apparently linear relation between ε and P and slopes of $\varepsilon(P)$ within 20%. Furthermore, the slope is consistent with a previous calibration of a one-dimensional random potential, when taking the different illuminated areas into account.¹⁹

In addition, the friction coefficient of the particles, ξ , implicitly depends on P . Due to hydrodynamic effects, the friction coefficient varies with the particles' distance from the water-glass interface.^{59,60,61} The distance is controlled by a balance between the repulsive particle-wall interaction^{63,64,65,66} and the radiation pressure,^{41,42,43} which pushes the particles toward the glass slide and depends on the laser power P . Thus, a finite $P > 0$ will lead to an increased friction coefficient and hence reduced diffusion coefficient. At short times the diffusion coefficient tends to a value, D_s , which can hence be used to guide the correction. Although the dynamics at short times are hardly affected by the random potential, the averaging over waiting times t_0 (Eq. 8) affects D_s .²⁰ This was considered when fitting the experimental value $D_s = D(t_s)$ (where $t_s \approx 0.2t_B$) to the corresponding simulation value. Moreover, we took into account that the choice of D_s affects t_B and in turn t_s and $D_s = D(t_s)$. This procedure provides the friction coefficient close to the water-glass interface; $\xi_0^* \approx 1.4\xi_0$ for $P > 0$ (and $\xi_0^* = \xi_0$ for $P = 0$ and the simulations). This implies an effective diffusion coefficient $D_0^*/D_0 = \xi_0/\xi_0^*$ and an effective Brownian time $t_B^*/t_B = \xi_0^*/\xi_0$ in the experiments with $P > 0$, while in the simulations (and experiments with $P = 0$) $D_0^* = D_0$ and $t_B^* = t_B$.

This procedure provides $\varepsilon(P)$ and corrects for radiation pressure effects, while fixing the diffusion coefficient $D(t)$ at short and long times. Nevertheless, the intermediate, subdiffusive behaviour is not affected and experimental and simulation results can be compared (Fig. 11). Agreement between experiments and simulations is found for $D(t)$, including intermediate times.

The diffusion coefficient at long times, D_∞ , has been linked to the free diffusion coefficient D_0 in the case of one-dimensional random potential energy landscapes with the values of the potential following a Gaussian distribution with

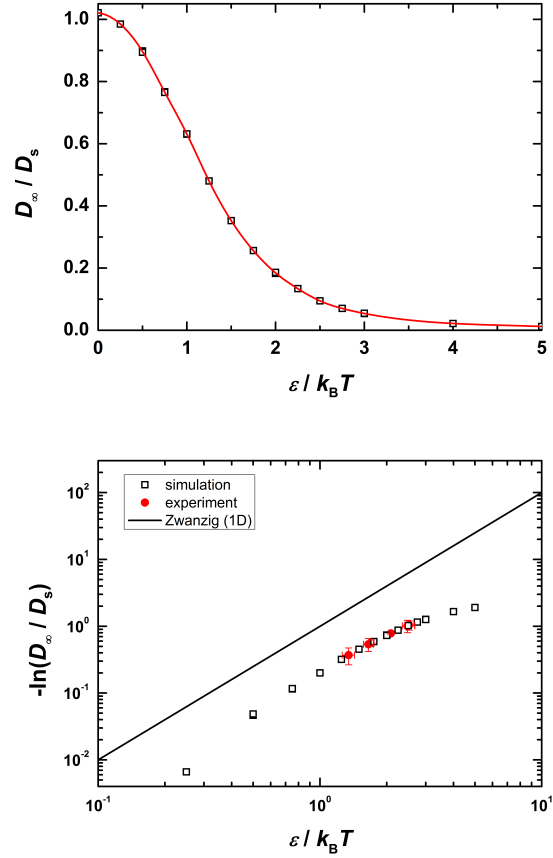


Fig. 12 Ratio of the long-time diffusion coefficient D_∞ and the short-time diffusion coefficient D_s as a function of degree of roughness ε in two different representations, as obtained from simulations (open squares) and experiments (filled circles, which are consistent with the simulation data by construction, Sec. 3.3). The lines represent (A) a spline interpolation and (B) a slope of two as expected for the case of a one-dimensional random potential energy landscape.¹⁶

width ε :¹⁶

$$\frac{D_\infty}{D_0} = e^{-(\varepsilon/k_B T)^2} \quad (11)$$

To our knowledge, theoretical predictions for higher dimensions are not available. Our simulation data (and, due to the procedure to link P to ε , also the experimental data) suggest a similar dependence at small values of ε (Fig. 12B). For large ε , however, we observe a significantly reduced decrease of D_∞/D_0 , i.e. a reduced slope in $-\ln(D_\infty(\varepsilon)/D_0)$ and thus an exponent below 2 in equation (11), maybe even a saturation. Therefore, for large ε , the dynamics appear not to slow down as strongly as in a one-dimensional system.^{16,19,20} This might be due to the possibility to avoid large barriers in

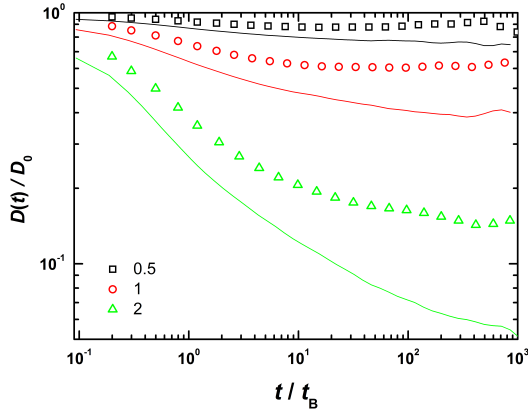


Fig. 13 Normalized diffusion coefficient $D(t)/D_0$ as a function of delay time t for particles in a one-dimensional (lines) and two-dimensional (symbols) random potential energy landscape with different standard deviations ϵ (as indicated) as observed in simulations.

two dimensions, which becomes increasingly attractive as ϵ grows. It might, however, also result from the fact that, with increasing ϵ , the system requires an increasingly long time to reach equilibrium and hence the average over waiting times is strongly weighted toward non-equilibrium states (which also affects D_s). Furthermore, with increasing ϵ it becomes increasingly difficult to determine D_∞ , i.e. the plateau of $D(t)$ at large times.

3.4 Comparison to particle dynamics in one-dimensional random and periodic potentials

The particle dynamics in one-dimensional random potential energy landscapes also show three distinct regimes; diffusion at short and long times and subdiffusion at intermediate times (Fig. 13).^{19,20} The dynamics are slower than in the two-dimensional case. In particular at long times, the dynamics are reduced and the long-time diffusive regime established at much longer times. In general, the characteristic times, for example t_μ and t_α , are longer and show a stronger dependence on ϵ .

In a periodic sinusoidal potential, only one barrier height exists and thus the distribution of escape times is narrower. Thus, the dynamics at intermediate times are more suppressed with a smaller slope at the inflection point of the mean squared displacement, corresponding to a deeper minimum of the exponent $\mu(t)$.⁵¹ On the other hand, long-time diffusion is established earlier.

4 Conclusions

We investigated the dynamics of individual colloidal particles in two-dimensional random potential energy landscapes, whose values follow a Gaussian distribution with a standard deviation ϵ , which characterizes the degree of roughness of the potential. In the experiments, the potential was created using an optical set-up and the roughness ϵ controlled via the laser power P . The relation $\epsilon(P)$ could be established with the help of Monte Carlo simulations. The experimentally observed dynamics agree with our simulation results. Three distinct regimes have been observed. At short times, the particles exhibit diffusive behaviour within their local minima, in which they remain until they cross a barrier, i.e. a saddle point, to a neighbouring minima. The wide distribution of barrier heights leads to a significant spread in residence times. This is reflected in the mean squared displacement as a broad subdiffusive region with a relatively large slope at the inflection point at intermediate times. At long times, the hopping between minima resembles a random walk and diffusive dynamics are recovered. The long-time diffusion coefficient decreases with increasing degree of roughness ϵ . For large ϵ this decrease is less pronounced than in one-dimensional potential energy landscapes.¹⁶ This is attributed to the possibility to bypass large barriers in two-dimensions, which is particularly utilized if large barriers are prevalent, i.e. for large ϵ .

The system presented here can also serve as a well-controlled, tunable and easily observable model for other systems, which either explore space or configuration space, i.e. a potential energy landscape. These systems include crowded systems, such as concentrated colloidal suspensions, supercooled liquids, glasses,^{30,31,32,33,34,35} or living cells,^{22,23,24} but also complex potential energy landscapes, such as those suggested in protein folding.^{36,37,38,39,40}

Acknowledgement

We thank Jürgen Horbach (University Düsseldorf) and Anand Yethiraj (Memorial University, Newfoundland) for very helpful discussions. Financial support from the International Helmholtz Research School of Biophysics and Soft Matter (IHRS BioSoft) and German Science Foundation (DFG) through the German-Dutch Collaborative Research Centre SFB-TR6 (Project Section C7) and the Research Unit FOR1394 (Project P8) is acknowledged.

References

- 1 M. D. Haw, *J. Phys.: Condens. Matter*, 2002, **14**, 7769–7779.
- 2 D. Babic, C. Schmitt and C. Bechinger, *Chaos*, 2005, **15**, 026114–6.
- 3 P. Hänggi and F. Marchesoni, *Chaos*, 2005, **15**, 026101–5.
- 4 I. M. Sokolov, *Soft Matter*, 2012, **8**, 9043–9052.
- 5 H. Löwen, *J. Phys.: Condens. Matter*, 2008, **20**, 404201.

- 6 A. van Blaaderen, *MRS Bulletin*, 2004, **29**, 85–90.
- 7 J.-P. Bouchaud and A. Georges, *Phys. Rep.*, 1990, **195**, 127–293.
- 8 D. S. Dean, I. T. Drummond and R. R. Horgan, *J. Stat. Mech.*, 2007, P07013.
- 9 S. Havlin and D. Ben-Avraham, *Adv. Phys.*, 1987, **36**, 695–798.
- 10 M. B. Isichenko, *Rev. Mod. Phys.*, 1992, **64**, 961–1043.
- 11 R. L. Jack and P. Sollich, *J. Stat. Mech.*, 2009, **2009**, P11011.
- 12 J. Bernasconi, H. U. Beyeler, S. Strässler and S. Alexander, *Phys. Rev. Lett.*, 1979, **42**, 819–822.
- 13 J. W. Haus, K. W. Kehr and J. W. Lyklema, *Phys. Rev. B*, 1982, **25**, 2905–2907.
- 14 D. S. Novikov, E. Fieremans, J. H. Jensen and J. A. Helpner, *Nat. Phys.*, 2011, **7**, 508–514.
- 15 H. Scher and M. Lax, *Phys. Rev. B*, 1973, **7**, 4491–4502.
- 16 R. Zwanzig, *Proc. Natl. Acad. Sci.*, 1988, **85**, 2029.
- 17 L. Chen, M. Falcioni and M. W. Deem, *J. Phys. Chem. B*, 2000, **104**, 6033.
- 18 F. Sciortino, *J. Stat. Mech.*, 2005, **2005**, P05015.
- 19 R. D. L. Hanes, C. Dalle-Ferrier, M. Schmiedeberg, M. C. Jenkins and S. U. Egelhaaf, *Soft Matter*, 2012, **8**, 2714–2723.
- 20 R. D. L. Hanes and S. U. Egelhaaf, *J. Phys.: Condens. Matter*, 2012, **24**, 464116.
- 21 R. M. Dickson, D. J. Norris, Y.-L. Tzeng and W. E. Moerner, *Science*, 1996, **274**, 966.
- 22 M. Weiss, M. Elsner, F. Kartberg and T. Nilsson, *Biophys. J.*, 2004, **87**, 3518–3524.
- 23 I. M. Tolić-Nørrelykke, E.-L. Munteanu, G. Thon, L. Oddershede and K. Berg-Sørensen, *Phys. Rev. Lett.*, 2004, **93**, 078102.
- 24 D. S. Banks and C. Fradin, *Biophys. J.*, 2005, **89**, 2960–2971.
- 25 A. Naumovets, *Physica A*, 2005, **357**, 189–215.
- 26 J. Barth, *Surf. Sci. Rep.*, 2000, **40**, 75–149.
- 27 P. Tierno, P. Reimann, T. H. Johansen and F. Sagués, *Phys. Rev. Lett.*, 2010, **105**, 230602.
- 28 A. Byström and A. M. Byström, *Acta Crystallogr.*, 1950, **3**, 146.
- 29 A. Heuer, S. Murugavel and B. Roling, *Phys. Rev. B*, 2005, **72**, 174304.
- 30 A. Heuer, *J. Phys.: Condens. Matter*, 2008, **20**, 373101.
- 31 P. G. Debenedetti and F. H. Stillinger, *Nature*, 2001, **410**, 259–267.
- 32 V. Lubchenko and P. G. Wolynes, *Annu. Rev. Phys. Chem.*, 2007, **58**, 235–266.
- 33 C. A. Angell, *Science*, 1995, **267**, 1924–1935.
- 34 W. C. K. Poon, *J. Phys.: Condens. Matter*, 2002, **14**, R859.
- 35 W. van Megen, T. C. Mortensen, S. R. Williams and J. Müller, *Phys. Rev. E*, 1998, **58**, 6073–6085.
- 36 R. B. Best and G. Hummer, *Phys. Chem. Chem. Phys.*, 2011, **13**, 16902–16911.
- 37 C. M. Dobson, A. Sali and M. Karplus, *Angew. Chem. Int. Ed.*, 1998, **37**, 868–893.
- 38 J. D. Bryngelson, J. N. Onuchic, N. D. Succi and P. G. Wolynes, *Proteins*, 1995, **21**, 167–195.
- 39 K. A. Dill and H. S. Chan, *Nat. Struct. Mol. Biol.*, 1997, **4**, 10–19.
- 40 R. Winter, D. Lopes, S. Grudzielanek and K. Vogt, *J. Non-Equilib. Thermodyn.*, 2007, **32**, 41–97.
- 41 A. Ashkin, *Proc. Natl. Acad. Sci.*, 1997, **94**, 4853–4860.
- 42 J. E. Molloy and M. J. Padgett, *Contemp. Phys.*, 2002, **43**, 241–258.
- 43 R. W. Bowman and M. J. Padgett, *Rep. Prog. Phys.*, 2013, **76**, 026401.
- 44 M. C. Jenkins and S. U. Egelhaaf, *J. Phys.: Condens. Matter*, 2008, **20**, 404220.
- 45 R. D. L. Hanes, M. C. Jenkins and S. U. Egelhaaf, *Rev. Sci. Instrum.*, 2009, **80**, 083703.
- 46 D. G. Grier, *Nature*, 2003, **424**, 810–816.
- 47 K. Dholakia and W. Lee, *Advances in Atomic, Molecular, and Optical Physics*, Academic Press, 2008, vol. 56, pp. 261–337.
- 48 K. Loudiyi and B. J. Ackerson, *Physica A*, 1992, **184**, 1–25.
- 49 Q.-H. Wei, C. Bechinger, D. Rudhardt and P. Leiderer, *Phys. Rev. Lett.*, 1998, **81**, 2606–2609.
- 50 C. Bechinger, Q. H. Wei and P. Leiderer, *J. Phys.: Condens. Matter*, 2000, **12**, A425.
- 51 C. Dalle-Ferrier, M. Krüger, R. D. L. Hanes, S. Walta, M. C. Jenkins and S. U. Egelhaaf, *Soft Matter*, 2011, **7**, 2064.
- 52 J. C. Crocker and D. G. Grier, *J. Colloid. Interface Sci.*, 1996, **179**, 298.
- 53 P. Habdas and E. R. Weeks, *Curr. Opin. Coll. Interf. Sci.*, 2002, **7**, 196–203.
- 54 C. Kreuter, P. Leiderer and A. Erbe, *Coll. Poly. Sci.*, 2012, **290**, 575–578.
- 55 M. Jenkins and S. Egelhaaf, *Adv. Colloid Interfac. Sci.*, 2008, **136**, 65.
- 56 R. W. Gerchberg and W. O. Saxton, *Optik*, 1972, **35**, 237.
- 57 J. W. Goodman, *Speckle Phenomena in Optics: Theory and Applications*, Roberts & Co Publ., 2010.
- 58 K. M. Douglass, S. Sukhov and A. Dogariu, *Nature Photonics*, 2012, **6**, 833–836.
- 59 E. S. Pagac, R. D. Tilton and D. C. Prieve, *Chem. Eng. Comm.*, 1996, **148–150**, 105–122.
- 60 J. Leach, H. Mushfique, S. Keen, R. Di Leonardo, G. Ruocco, J. M. Cooper and M. J. Padgett, *Phys. Rev. E*, 2009, **79**, 026301.
- 61 P. Sharma, S. Ghosh and S. Bhattacharya, *Appl. Phys. Lett.*, 2010, **97**, 104101.
- 62 B. Vorselaars, A. V. Lyulin, K. Karatasos and M. A. J. Michels, *Phys. Rev. E*, 2007, **75**, 011504.
- 63 W. A. Ducker, T. J. Senden and R. M. Pashley, *Nature*, 1991, **353**, 239.
- 64 S. G. Flicker, J. L. Tipa and S. G. Bike, *J. Colloid Interface Sci.*, 1993, **158**, 317.
- 65 J. Y. Walz, *Curr. Opin. Colloid Interface Sci.*, 1997, **2**, 600.
- 66 H. H. von Grünberg, L. Helden, P. Leiderer and C. Bechinger, *J. Chem. Phys.*, 2001, **114**, 10094–10104.